Z. Phys. Chem. **226** (2012) 525–537 / **DOI** 10.1524/zpch.2012.0250

Li Ion Dynamics in Al-Doped Garnet-Type $Li_7La_3Zr_2O_{12}$ Crystallizing with Cubic Symmetry

By Alexander Kuhn[1,*], Joon-Yong Choi[2], Lars Robben[3], Frank Tietz[2], Martin Wilkening[4], and Paul Heitjans[1]

[1] Leibniz University Hannover, Institute of Physical Chemistry and Electrochemistry, and ZFM – Center for Solid State Chemistry and New Materials, Callinstr. 3a, 30167 Hannover, Germany
[2] Institute of Energy and Climate Research (IEK-1), Forschungszentrum Jülich GmbH, 52425 Jülich, Germany
[3] Leibniz University Hannover, Institute of Mineralogy, Callinstr. 3, 39167 Hannover, Germany
[4] Graz University of Technology, Institute for Chemistry and Technology of Materials, Stremayrgasse 9, 8010 Graz, Austria

(Received April 13, 2012; accepted in revised form May 18, 2012)
(Published online June 18, 2012)

Solid Electrolytes / Garnets / Lithium Ion Dynamics / NMR / Spin-Lattice Relaxation

Lithium-ion dynamics in the garnet-type solid electrolyte "$Li_7La_3Zr_2O_{12}$" (LLZ) crystallizing with cubic symmetry was probed by means of variable-temperature ^{7}Li NMR spectroscopy and ac impedance measurements. Li jump rates of an Al-containing sample follow Arrhenius behavior being characterized by a relatively high activation energy of 0.54(3) eV and a pre-exponential factor of $2.2(5) \times 10^{13}$ s^{-1}. The results resemble those which were quite recently obtained for an Al-free LLZ sample crystallizing, however, with tetragonal symmetry. Hence, most likely, the significantly higher Li conductivity previously reported for a cubic LLZ sample cannot be ascribed solely to the slight structural distortions accompanying the change of the crystal symmetry. Here, even Al impurities, acting as stabilizer for the cubic polymorph at room temperature, do not lead to the high ion conductivity reported previously.

1. Introduction

In recent years, Li containing garnets have attracted large interest due to their potential usage as electrolytes in all-solid-state Li secondary batteries [1–8]. The high lithium-ion conductivity of such ceramics showing good electrochemical stability to lithium metal makes them promising candidates to be used, for example, in thin-film batteries [9].

* Corresponding author. E-mail: kuhn@pci.uni-hannover.de

In particular, garnet-type $Li_7La_3Zr_2O_{12}$ (LLZ) crystallizing with cubic symmetry has captured the attention of the materials science community due to its extraordinarily high room-temperature lithium-ion conductivity which is 3×10^{-4} S cm^{-1} [10]. Interestingly, the corresponding Li conductivity of the tetragonal modification [11] is only 1.6×10^{-6} S cm^{-1}. However, the structural differences of the two modifications are rather small with respect to the garnet-type network $[La_3Zr_2O_{12}]^{-7}$ [11,12]. This raises the question whether the distortion of the lattice, which amounts to less than 2%, is solely responsible for the large difference in ion conductivity observed. Quite recently, Geiger *et al.* assumed that traces of Al ions incorporated during the high-temperature synthesis of cubic LLZ play an important role in the enhancement of the conductivity observed [12]. Note that an Al-containing sample of cubic LLZ, which was complementarily investigated by some of us using impedance measurements and NMR spectroscopy [13], indeed showed the extremely high lithium-ion conductivity mentioned above. Doping with Al might create additional vacancies at the regularly occupied Li sites, for example. However, in view of the large fraction of unoccupied Li sites already present in (phase-pure) cubic LLZ [12], the effect of additionally generated Li vacancies on the Li ion conductivity might be too small to solely account for the enhancement found.

Irrespective of such an effect, evidences have been found that the Al^{3+} ions incorporated do stabilize the cubic modification relative to the tetragonal one [12]. Whereas an Al-free sample with cubic symmetry is reported to be the non-quenchable high-temperature form [12], the tetragonal modification can be obtained at much lower synthesis temperatures [11,14] or, alternatively, by the use of Pt crucibles, for example [12]. In agreement with these observations, Al-free tetragonal LLZ reversibly transforms into the cubic polymorph at elevated temperatures as reported recently [12,14]. However, as has been shown by some of us [14], no change in ion conductivity is associated with this phase transformation. This indicates that the slight structural changes coming along with the increase of the symmetry do not alter the Li transport parameters significantly. These readily follow a single Arrhenius line over a large dynamic range of several orders of magnitudes [14].

Whereas the studies available so far give evidences that incorporation of Al is beneficial to stabilize the cubic modification at room temperature as mentioned above, the corresponding influence on lithium ion dynamics is still unclear. The investigations published until now bring up the question whether the increased ion conductivity observed can solely be ascribed to Al doping. In the present study, lithium-ion dynamics of an LLZ sample, which is slightly contaminated with Al ions, is comprehensively studied by both time-domain ^{7}Li NMR measurements and ac impedance spectroscopy, *i. e.*, from a microscopic and macroscopic point of view [15–17]. The results are compared with those of an Al-free sample crystallizing with tetragonal symmetry [11,14]. Surprisingly, although the sample studied here expectedly shows the typical X-ray powder pattern of a garnet crystallizing with cubic symmetry, the lithium-ion conductivity turns out to be rather low and is very similar to that of the (Al-free) tetragonal modification [11,14]. Thus, stabilization of the cubic modification by appropriate doping with a trivalent cation such as Al might be not the only reason of the enhanced conductivity found in some of the LLZ samples studied so far.

2. Experimental

$Li_7La_3Zr_2O_{12}$ crystallizing with cubic symmetry was prepared by a conventional solid-state reaction. Highly pure Li_2CO_3, ZrO_2 and La_2O_3 were used as starting materials. With regard to the stoichiometric mixture, an excess of 10 wt. % of Li_2CO_3 was used to compensate for any Li loss expected at high temperatures. After grinding, the materials were placed in an alumina crucible and calcined at 1253 K for several hours and, following a second grinding step, heated at 1500 K for 1 h once again. The amount of Al introduced into the sample during this procedure has been determined by inductively coupled plasma optical emission spectroscopy (ICP-OES 750, Varian) to be 1.1 wt. %.

X-ray powder diffraction (XRPD) data were recorded on a Bruker D4 Endeavor diffractometer using a reflection geometry, Cu $K_{\alpha 1,2}$ radiation and a secondary Ni filter. 4000 data points were collected with a step width of 0.02° in the 2Θ range from 10 to 90°. XRPD data were analyzed by TOPAS 4.2 (Bruker AXS) software. During refinements, the general parameters such as scale factors, background parameters and zero point errors were optimized. Profile shape calculations were carried out on the basis of standard instrumental parameters using the fundamental parameter approach implemented in the program, also varying the average crystal size (integral breadth) of the reflections. The phases have been considered in the total pattern calculations either as crystal structures or *hkl* phases. Energy-dispersive X-ray (EDX) mapping was performed with a Jeol 6390 scanning electron microscope equipped with a JEOL JED-2300 Analysis Station in order to get insight into the elemental distribution in different crystallites.

Static ^{7}Li NMR line shape and spin-lattice relaxation (SLR) rate measurements were performed with a modified Bruker MSL 100 and an MSL 400 spectrometer each connected to an Oxford cryomagnet with nominal fields of 4.7 T and 9.4 T, respectively. Both commercial and home-built probes (designed for high temperatures) were used. ^{7}Li SLR NMR rates were recorded with the standard saturation recovery pulse sequence, $10 \times \pi/2 - t_{delay} - \pi/2 -$ acquisition, using 14 different delay times t_{delay}. The magnetization transients were in satisfying agreement with single-exponential relaxation. Alternatively, the transients were fitted with stretched exponentials in order to account for small deviations from single-exponential behavior. The rates obtained from the two fits yielded comparable results.

High-resolution, *i. e.*, magic angle spinning (MAS), ^{27}Al and ^{6}Li NMR measurements were performed on an Avance III spectrometer (Bruker) connected to a Bruker cryomagnet with a nominal field of 14.1 T. A commercial 2.5 mm-MAS probe (Bruker) was employed which allowed spinning speeds of up to 30 kHz. NMR spectra were referenced to an 1N aqueous solution of $Al(NO_3)_3$.

Ac impedance measurements were performed with a Novocontrol impedance spectrometer Concept 80 equipped with a BDS 1200 sample cell and an Alpha analyzer (Novocontrol) in the frequency range from 0.1 Hz to 10 MHz. Impedance spectra were recorded at temperatures ranging from 198 K to 523 K. Pt electrodes were applied to the non-sintered pellets which were 8 mm in diameter and approximately 1 mm in thickness. The measurements were performed under a stream of heated nitrogen. Prior to the first measurement, the sample was dried at 523 K for 30 min in order to remove any moisture.

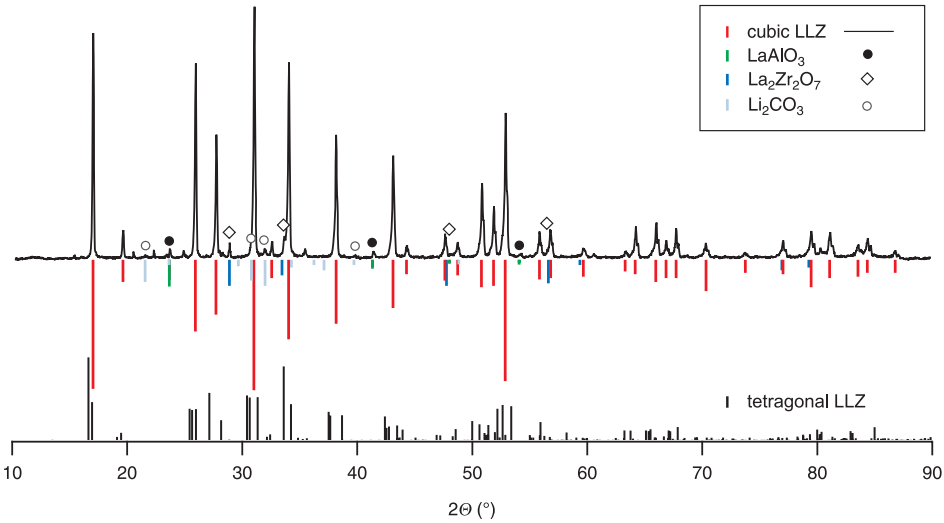

Fig. 1. XRD pattern of the cubic LLZ sample investigated which contains a small amount of Al. The main peaks of the impurities detected ($LiAlO_3$, $Li_2Zr_2O_7$, Li_2CO_3) are additionally highlighted (see legend). Note that these do overlap with some of the peaks of LLZ. For comparison, the XRD pattern of tetragonal LLZ according to Ref. [11] is shown.

3. Results and discussion

3.1 Sample characterization

3.1.1 X-ray powder diffraction

Analysis of the XRPD pattern of the prepared LLZ sample (Fig. 1) reveals the cubic modification as described by Geiger *et al.* [12] to be the main phase with a content of approximately 97 wt. %. Some additional peaks with low intensity point to impurities such as $La_2Zr_2O_7$, $LaAlO_3$, and Li_2CO_3. The actual amount of Li_2CO_3 determined by Rietveld analysis is uncertain due to the low crystallinity of the sample which leads to rather broad peak widths.

3.1.2 ^{27}Al and ^{6}Li MAS NMR spectra

In order to further characterize the prepared sample and to study its structure from an atomic-scale point of view, ^{27}Al and ^{6}Li MAS NMR spectra were recorded at ambient bearing gas temperature. In Fig. 2, ^{27}Al MAS NMR spectra of cubic LLZ with about 1.1 wt. % Al and the Al-free tetragonal LLZ studied recently [14] are shown. While the latter does not reveal any ^{27}Al NMR intensities, the first is composed of at least three different lines showing up at 12 ppm, 64 ppm, and 80 ppm. The signal with an isotropic chemical shift of $\delta = 12$ ppm indicates Al ions residing in octahedral sites. Thus, most likely, it can be attributed to $LaAlO_3$ which has also been detected by XRPD (see above and the study by Geiger *et al.* [12]) The NMR intensities showing up at approximately 65 ppm and 80 ppm point to tetrahedrally coordinated Al ions [18] in the LLZ structure. Most probably, the broad signal at 65 ppm reflects Al ions on the Li(1) site in cubic

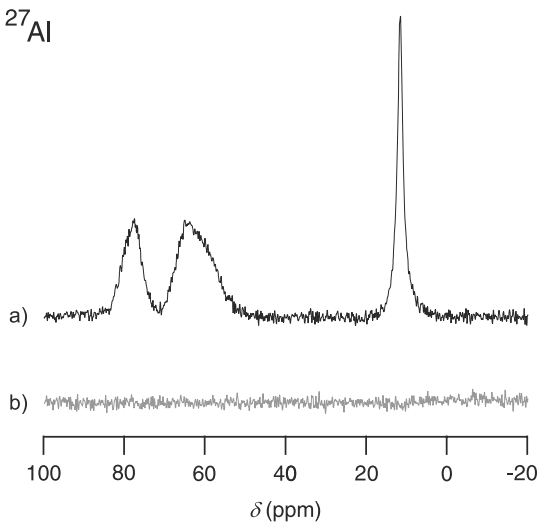

Fig. 2. a) ^{27}Al MAS NMR spectrum of the (Al-doped) cubic LLZ sample investigated. The spectrum was recorded at 14.1 T using an MAS spinning speed of 30 kHz. While the line at 12 ppm might be attributed to $LaAlO_3$, the intensities showing up in the range from 50 to 90 ppm indicate Al ions incorporated into LLZ. b) For comparison, the ^{27}Al MAS NMR spectrum of the Al-free tetragonal LLZ sample [14] is also presented.

LLZ [12] while the line with a larger chemical shift value might be related to the replacement of La and Zr by Al [19]. Most likely, Al resides on a tetrahedral site near a La or Zr vacancy. In order to further check the distribution of Al in the different phases occurring in the sample, an EDX elemental mapping was performed using a SEM microscope equipped with a JEOL JED-2300 Analysis Station. The results are shown in Fig. 3. The large particle contains La, Zr and traces of Al and most probably is the LLZ phase. Smaller particles show higher amounts of Al and La and probably resemble the $LaAlO_3$ minor phase.

The ^{6}Li MAS NMR spectrum of cubic LLZ (not shown here) is composed of two lines which are characterized by quite different NMR SLR rates. The main line at 1.1 ppm (referenced to 1 N aqueous LiCl), comprising approximately 90% of the total integral, presumably reflects the Li ions in LLZ while the minor component at -0.1 ppm might be attributed to a separate phase such as Li_2CO_3 as detected by XRPD (see above). Additionally, carbonate modes are also seen in the corresponding transmission infrared (IR) spectra recorded. At room temperature the corresponding ^{6}Li NMR spin-lattice relaxation time is in the order of 1000 s whereas that of the main component is less than 10 s. Li_2CO_3 might either stem from the preparation route chosen or from the reaction with ambient air as also found in the case of lithium lanthanum titanate (LLT) [20]. Note that the replacement of Li^+ by H^+, which is the key reaction for the formation of Li_2CO_3 in the case of LLT, was reported at least for the related garnet-type electrolytes $Li_5La_3Nb_2O_{12}$ and $Li_5La_3Ta_2O_{12}$ [21]. IR spectra in the mentioned work revealed the characteristic bands of carbonate ions. Interestingly, Nyman *et al.* [21] showed that the ^{6}Li MAS NMR line in question, which shows up at approxi-

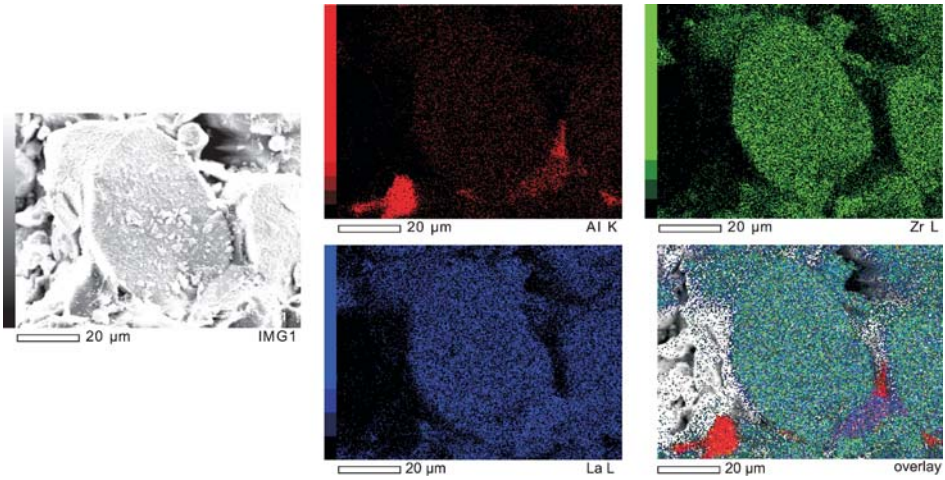

Fig. 3. Left: SEM micrograph of the cubic LLZ sample. Right: EDX mapping (JEOL JED-2300 Analysis Station) of the same image section for the elements Al, La, and Zr. The overlay of the elemental distribution is also included.

mately 0.2 ppm, disappears when the sample is treated with acids. Concomitantly, the IR bands reflecting the carbonate modes disappear.

3.2 Bulk ion conductivity

Unlike the case of NMR SLR measurements, small amounts of impurities such as Li_2CO_3, when located on the surface of the grains, might affect the resistance attributed to the grain boundary regions. However, the respective impact on the bulk conductivities might be less significant as long as the grains are large enough and the volume fraction of the insulating impurities is low. Here, bulk conductivities (see Fig. 4) of the cubic sample were read out from the frequency-independent plateau showing up at higher frequencies in the corresponding conductivity isotherms [14].

The conductivity spectra were constructed by plotting the real part of the conductivity σ' *vs.* frequency f. The plateau analyzed here is related to the process with the lowest capacity; it reflects the electrical response of the bulk. In Fig. 4 the corresponding bulk conductivities of cubic LLZ are shown (red dots). At room temperature the ion conductivity amounts to $3(1) \times 10^{-7}$ S/cm. The activation energy derived from the Arrhenius plot shown turns out to be 0.53(2) eV.

For comparison, literature data of cubic and Al-free tetragonal LLZ [14] are also included in Fig. 4. The conductivities probed here are in very good agreement with those of the tetragonal sample studied by Awaka *et al.* [11]. However, significant differences become apparent when the present data are compared with the results reported by Murugan *et al.* [10] for cubic LLZ. Thus, although the sample investigated crystallizes with cubic symmetry, no enhancement is found compared to the tetragonal form. Even more important, the incorporated Al ions seem to have no effect on the Li mobility.

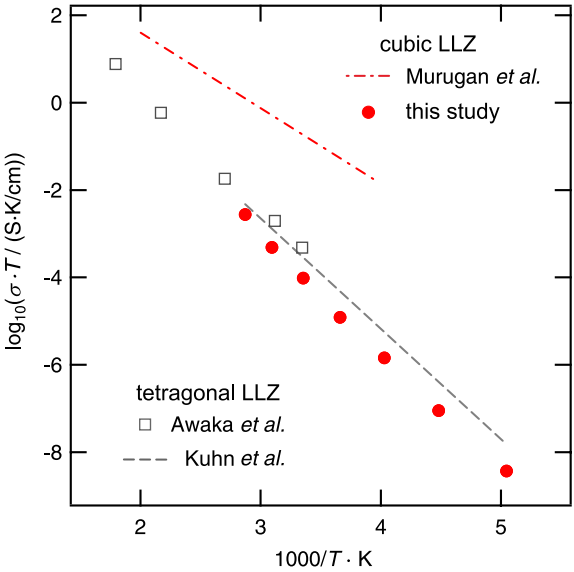

Fig. 4. Temperature dependence of the bulk lithium-ion conductivities of Al-doped, cubic LLZ (plotted as $\log_{10} \sigma T$ *vs.* temperature). For comparison, literature data for cubic [10] and tetragonal LLZ [11,14] are also shown.

3.3 Variable-temperature ^{7}Li NMR line shapes

In addition to impedance spectroscopy, static ^{7}Li NMR lines (see Fig. 5a) were recorded to study the Li diffusivity in the cubic sample prepared. At low temperatures, the lines are dipolarly broadened and show a Gaussian shape. With rising temperature the Li jump rate τ^{-1} increases. At a given temperature, here at approximately 290 K, τ^{-1} becomes comparable to the dipolar coupling constant. Dipolar interactions are then increasingly averaged resulting in the so-called motional narrowing (MN) of the NMR line. At high temperatures, *i. e.*, in the regime of extreme narrowing, the line width simply reflects the inhomogeneity of the external magnetic field used. The two-component line shape showing up in the intermediate T range might indicate heterogeneous dynamics taking place in the cubic sample. Alternatively such effects might be explained by coupling of the spins with paramagnetic impurities leading in some cases to a slight line broadening [23]. As expected for cubic symmetry, the NMR line recorded at high temperatures (533 K) does not reveal any indications for satellite transitions (see Fig. 5a). Note that this is in contrast to the tetragonal sample studied recently [14]. In general, at high temperatures the fast diffusing Li ions are exposed to a mean electric field gradient (EFG) of all visited sites. This leads to a vanishing mean EFG in the case of cubic LLZ and a non-vanishing one in tetragonal LLZ. Incorporation of isotropically distributed dopant atoms such as Al is expected not to change this situation.

As pointed out above, the temperature-dependent narrowing of the NMR (central) transition line can be used to roughly estimate the Li diffusivity. In Fig. 5b the resulting MN curve is shown, which is obtained by plotting the line width (full width at half maximum *fwhm*) *vs.* temperature. Obviously, the data points are very similar to those of

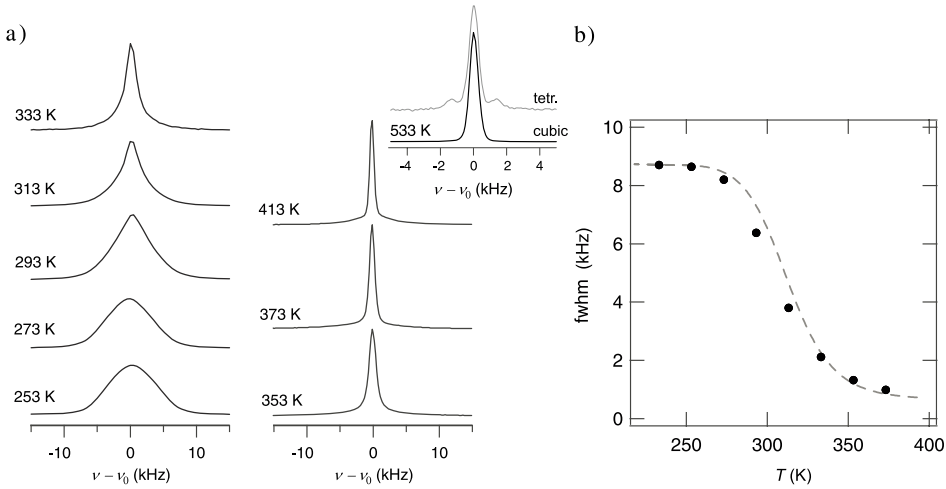

Fig. 5. a) Temperature-dependent static ^{7}Li NMR lines of the Al-doped, cubic sample of LLZ. Inset: The spectrum recorded at 553 K does not reveal any quadrupole satellites as expected for a material with cubic symmetry. For comparison, the spectrum of tetragonal LLZ (533 K) which shows quadrupole satellites is included (grey line) [14]. See text for further explanation. b) Motional narrowing (MN) of the central transition of the ^{7}Li NMR line of cubic LLZ (black dots). The dashed line, shown for comparison, represents a fit [22] through the MN data of the tetragonal modification of LLZ studied recently [14].

the Al-free sample crystallizing with tetragonal symmetry. This result corroborates the similarity of the two samples found by impedance spectroscopy presented above. At the temperature of the inflection point the mean Li jump rate is given by $\Delta\omega_{\text{rigid lattice}} \approx \tau^{-1}$ where $\Delta\omega_{\text{rigid lattice}}/2\pi$ refers to the line width in the rigid lattice regime. Here, τ^{-1} amounts to approximately 5.5×10^4 s^{-1} at 300 K.

3.4 ^{7}Li NMR relaxometry

A more detailed insight into the Li ion dynamics in solid electrolytes can be obtained by variable-temperature NMR relaxometry [14,24–28]. Provided the jump rates follow a single Arrhenius law

$$\tau^{-1} = \tau_0^{-1} \cdot \exp\left(-\frac{E_A}{k_B T}\right) \tag{1}$$

then the same diffusion process can be studied over a wide dynamic range being tantamount to a wide temperature range. Here, k_B denotes Boltzmann's constant. Whereas NMR SLR rate (R_1) measurements performed in the laboratory frame are sensitive to jump rates in the order of $\tau^{-1} \approx 10^9$ s^{-1}, lower values of τ^{-1} (approximately 10^5 s^{-1}) can be probed by SLR rate measurements carried out in the rotating frame of reference ($R_{1\rho}$). Typical locking frequencies of the latter are of the order of some tens of kHz. Here, the combination of the two methods [14,29] yields a comprehensive picture of the Li dynamics taking place in cubic LLZ.

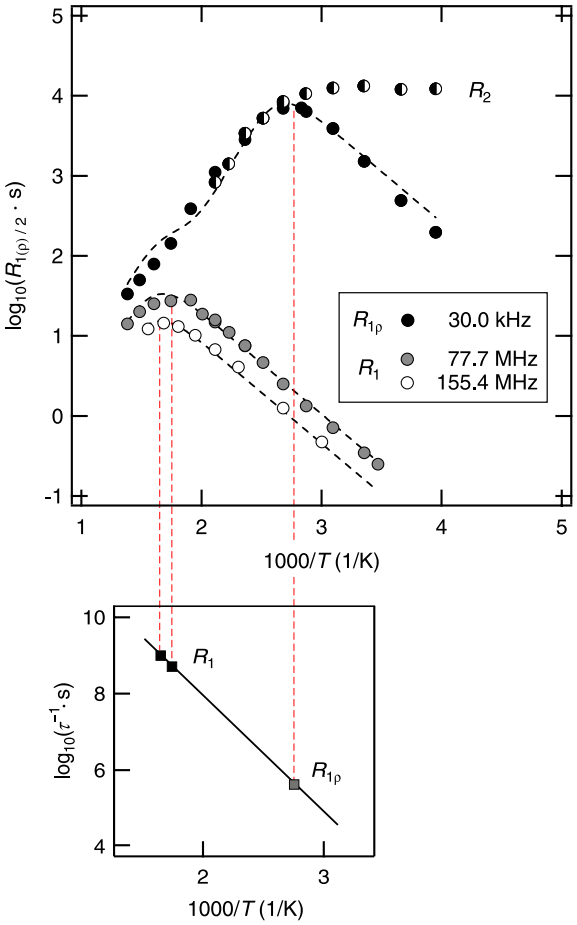

Fig. 6. Top: Arrhenius plot of the ^{7}Li NMR SLR rates of Al-doped LLZ. The rates were probed in both the laboratory frame (R_1) and in the rotating frame $R_{1\rho}$ of reference. For comparison, ^{7}Li NMR spin-spin relaxation rates (R_2) are shown, too. Bottom: Arrhenius plot of the Li jump rates extracted solely from the SLR rate maxima.

In Fig. 6, ^{7}Li NMR SLR rates R_1 measured at two different Larmor frequencies ($\omega_0/2\pi = 77.7$ MHz and $\omega_0/2\pi = 155.4$ MHz) are shown in an Arrhenius plot. The corresponding SLR rates $R_{1\rho}$, measured in the rotating frame of reference at a locking frequency $\omega_{\text{lock}}/2\pi$ of 30.0 kHz, are also included in Fig. 6. The R_1 rates pass through a maximum at rather elevated temperatures, *i. e.*, slightly above 570 K. From each rate maximum, an absolute Li jump rate can be calculated using the maximum condition $\tau^{-1} \approx \omega_0$ [24]. For the $R_{1\rho}$ rate peak, the maximum condition $\tau^{-1} \approx 2\omega_{\text{lock}}$ holds [30]. The so obtained Li jump rates are shown in the Arrhenius plot of Fig. 6 (bottom). The solid line represents a fit according to Eq. 1 and yields $E_A = 0.59(4)$ eV. Here, the error given is estimated from the uncertainty of the exact positions of the diffusion-

induced rate maxima. The value is in fair agreement with that probed by impedance spectroscopy (*vide supra*).

A more detailed analysis of the NMR relaxometry data collected includes a joint fit requiring a suitable relaxation model. According to the model of Bloembergen, Purcell and Pound [24] developed for 3D isotropic diffusion (of spin-1/2 nuclei), in the case of homonuclear dipolar relaxation the SLR rates R_1 and $R_{1\rho}$ are given by [23,31]

$$R_1 = M_2 \cdot \left[\tfrac{1}{3} j(\omega_0) + \tfrac{4}{3} j(2\omega_0)\right], \tag{2}$$

$$R_{1\rho} = M_2 \cdot \left[\tfrac{1}{2} j(2\omega_1) + \tfrac{5}{6} j(\omega_0) + \tfrac{1}{3} j(2\omega_0)\right]. \tag{3}$$

Here, M_2 is the second moment of the interaction in the rigid lattice and

$$\omega_1 = \sqrt{\omega_{\text{lock}}^2 + \omega_{\text{local}}^2}$$

denotes the effective locking frequency where ω_{local} represents the frequency corresponding to the local internal field. $j(\omega)$ is the Fourier transform of the normalized NMR correlation function $g(t)$ which decays from 1 to 0. $g(t)$ describes the random fluctuations of an interaction due to motional processes of the spins. If the motional process is a Brownian one, *i. e.*, assuming the jump process is uncorrelated, the correlation function can be represented by a single exponential decay function

$$g(t) = \exp[-t/\tau_c] \tag{4}$$

where τ_c is the motional correlation time. Deviations from uncorrelated motion can often be sufficiently well described by replacing the single exponential by a stretched exponential one. This is independent of the assumed nature of the microscopic reason of the correlation such as structural disorder, Coulomb interactions or the presence of cooperative motion. Hereby, the stretching parameter $0 < \beta \leq 1$ is introduced.

$$g(t) = \exp[-(t/\tau^*)^\beta] \tag{5}$$

There is no general analytical expression for the Fourier transform of the stretched exponential function but the following expression is a good approximation (with τ and $\langle\tau_c\rangle = \frac{\tau^*}{\beta} \cdot \Gamma\left(\frac{1}{\beta}\right)$ being of the same order of magnitude):

$$j(\omega) = \frac{2\tau}{1 + (\omega\tau)^{1+\beta}}. \tag{6}$$

Equations 1, 2 and 6 can be used to fit the NMR relaxometry data with the only fit parameters being (i) those describing the Arrhenius-activated jump process τ_0 and E_A, (ii) the stretching exponent β, and (iii) the external and internal experimental parameters. The latter include the NMR frequencies used, the local field ω_{local}, and the interaction strength M_2 of the fluctuating interaction which is responsible for the relaxation process.

Here, the obtained ratio $R_1(^7\text{Li})/R_1(^6\text{Li}) \approx 2$ points to a dipolar relaxation mechanism. Interestingly, the interaction strength for dipolar interaction between ^{7}Li nuclei,

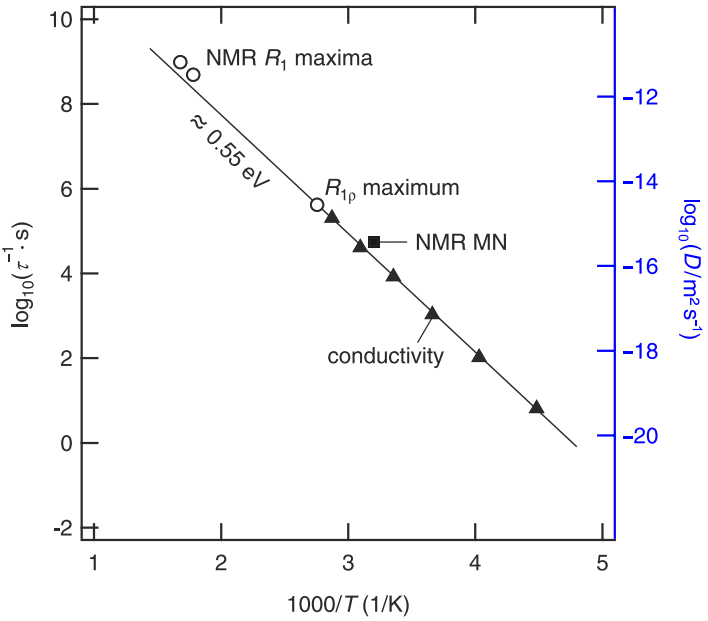

Fig. 7. Li jump rates (left axis) and diffusion coefficients (right axis) of Al-doped cubic LLZ. The rates were obtained from bulk conductivity and ^{7}Li NMR measurements as indicated. The solid line shows an Arrhenius fit yielding an activation energy of approximately 0.55 eV and a pre-exponential factor of 2×10^{13} s^{-1}.

which is obtained from spin-spin relaxation rate (R_2) measurements (see Fig. 6) carried out in the rigid lattice regime, is too low to explain the absolute value of the rates. This difference might be ascribed to a relaxation mechanism governed by dipolar interactions of the diffusing ^{7}Li spins with immobile paramagnetic impurities [23]. The corresponding interaction strength is expected to be higher due to the much larger magnetic moment of the relaxation center. Besides this difference observed, the diffusion-induced ^{7}Li NMR SLR rates recorded in the laboratory and rotating frames of reference do not seem to coincide at high temperatures. Here, the found ratio of $R_{1\rho}/R_1 = 4$ also points to the assumed relaxation mechanism taking into account the spin-quantum number $I = 3/2$ of ^{7}Li, see [23,32].

The assumption of relaxation at paramagnetic centers is also in agreement with the observation that the $R_{1\rho}(1/T)$ rate peak cannot be satisfactorily well fitted with $\omega_1 = (\omega_{\text{lock}}^2 + \omega_{\text{local}}^2)^{1/2}$, *i. e.*, when solely homonuclear ^{7}Li–^{7}Li dipole interactions are considered. Replacing ω_1 with $\omega_{1\,\text{eff}}$, corresponding to an effective field, does yield a reasonable fit. Here, $\omega_{1\,\text{eff}}$ can be estimated from a comparison of the R_1 and R_2 rates (Fig. 6), and it turned out that it is of the same order of magnitude as the pulsed locking field.

Taking these parameters, a joint fit can be performed with only three free variables being τ_0, E_A and β which fully describe the motional process. In Fig. 6, the joint fit is indicated as dashed lines yielding $E_A = 0.55$ eV, $\tau_0 = 2.2 \times 10^{13}$ s^{-1} and $\beta = 0.45$.

3.5 Comparison of conductivity data and NMR results

Finally, in order to compare conductivity data with those deduced from NMR, the conductivity values probed have to be converted into jump rates using both the Nernst-Einstein equation and the Einstein-Smoluchowski equation. A combination of the two yields

$$\tau^{-1} = H_R/f \cdot \frac{6\sigma_{DC}k_BT}{Nq^2a^2}\,. \tag{7}$$

H_R is the Haven ratio and f denotes the correlation factor, see *e. g.* Ref. [17]. Here, H_R/f is assumed to be 1. N is the charge carrier density and q is the charge of the Li ions. a denotes the jump distance estimated from the crystal structure. In Fig. 7, the so obtained jump rates τ^{-1} are shown in an Arrhenius plot together with those deduced from NMR. Obviously, the two methods are sensitive to the same motional process. Taken together, Li diffusion in cubic LLZ turned out to be characterized by $E_A \approx 0.54(3)$ eV and $\tau_0^{-1} \approx 2.2(5) \times 10^{13}$ s^{-1}. Interestingly, these values are very similar to those recently reported for the tetragonal modification of LLZ [14].

4. Conclusions

Dynamic parameters of Li dynamics in $Li_7La_3Zr_2O_{12}$ crystallizing with cubic symmetry were studied by both impedance spectroscopy and ^{7}Li NMR relaxometry. The sample was prepared in alumina crucibles at high temperatures; it contains a small amount of aluminium which has been detected by ^{27}Al MAS NMR. Presumably, the incorporated Al stabilizes the *cubic* modification. Impedance data and NMR SLR rates point to the same Arrhenius-type transport process being characterized by $E_A \approx 0.54(3)$ eV and a pre-exponential factor of $\tau_0^{-1} \approx 2.2(5) \times 10^{13}$ s^{-1}. Interestingly, the same result was obtained for phase-pure (Al-free) LLZ crystallizing with *tetragonal* symmetry. Therefore, in the present case neither the change in crystal symmetry nor the fact that Al has been incorporated leads to the enhancement of the Li ion conductivity as found for other (Al-doped) samples, recently. This indicates that the reasons for the enhancement in ionic conductivity observed in some cases are still unclear. Presumably, the oxygen stoichiometry might also influence the ion conductivity which has to be taken into account in further experimental studies to elucidate Li dynamics in garnet-type LLZ.

Acknowledgement

We thank Marc Krey for the ICP-OES analysis. Financial support by the Federal Ministry of Education and Science (BMBF) within the framework of the "Kompetenzverbund Nord" and by the Deutsche Forschungsgemeinschaft (DFG) *via* the Research Unit 1277 (molife) is gratefully acknowledged. A. K. acknowledges support by the Studienstiftung des deutschen Volkes e.V.

References

1. V. Thangadurai, H. Kaack, and W. Weppner, J. Am. Chem. Soc. **86** (2003) 437.
2. V. Thangadurai and W. Weppner, Adv. Funct. Mater. **15** (2005) 107.
3. V. Thangadurai and W. Weppner, J. Power Sources **142** (2005) 339.
4. A. Ramzy and V. Thangadurai, Appl. Mater. Interfaces **2** (2010) 385.
5. L. v. Wüllen, T. Echelmeyer, H.-W. Meyer, and D. Wilmer, Phys. Chem. Chem. Phys. **9** (2007) 3298.
6. B. Koch and M. Vogel, Solid State Nucl. Magn. **34** (2008) 37.
7. E. J. Cussen, Chem. Commun. (2006) 412.
8. E. J. Cussen, J. Mater. Chem. **20** (2010) 5167.
9. M. Kotobuki, H. Munakata, K. Kanamura, Y. Sato, and T. Yoshida, J. Electrochem. Soc. **157** (2010) A1076.
10. R. Murugan, V. Thangadurai, and W. Weppner, Angew. Chem. Int. Edit. **46** (2007) 7778.
11. J. Awaka, N. Kijima, H. Hayakawa, and J. Akimoto, J. Solid State Chem. **182** (2009) 2046.
12. C. A. Geiger, E. Alekseev, B. Lazic, M. Fisch, T. Armbruster, R. Langner, M. Fechtelkord, N. Kim, T. Pettke, and W. Weppner, Inorg. Chem. **50** (2011) 1089.
13. H. Buschmann, J. Dölle, S. Berendts, A. Kuhn, P. Bottke, M. Wilkening, P. Heitjans, A. Senyshyn, H. Ehrenberg, A. Lottnyk, V. Duppel, L. Kienle, and J. Janek, Phys. Chem. Chem. Phys. **13** (2011) 19378.
14. A. Kuhn, S. Narayanan, L. Spencer, G. Goward, V. Thangadurai, and M. Wilkening, Phys. Rev. B **83** (2011) 094302.
15. S. Narayanan, V. Epp, M. Wilkening, and V. Thangadurai, RSC Adv. **2** (2012) 2553.
16. M. Wilkening and P. Heitjans, Chem. Phys. Chem. **13** (2012) 53.
17. P. Heitjans and S. Indris, J. Phys.-Condens. Mat. **15** (2003) R1257.
18. K. J. D. MacKenzie and M. E. Smith, *Multinuclear Solid-State NMR of Inorganic Materials*, Elsevier, Oxford (2002).
19. A. Düvel, A. Kuhn, L. Robben, M. Wilkening, and P. Heitjans, J. Phys. Chem. C submitted (2011).
20. A. Boulant, J. F. Bardeau, A. Jouanneaux, J. Emery, J.-Y. Buzare, and O. Bohnke, Dalton T. **39** (2010) 3968.
21. M. Nyman, T. M. Alam, S. K. McIntyre, G. C. Bleier, and D. Ingersoll, Chem. Mater. **22** (2010) 5401.
22. J. Hendrickson and P. Bray, J. Magn. Reson. **9** (1973) 341.
23. P. M. Richards, Top. Curr. Phys. **25** (1979) 1019.
24. N. Bloembergen, E. Purcell, and R. Pound, Phys. Rev. **73** (1948) 679.
25. D. Ailion and C. P. Slichter, Phys. Rev. Lett. **12** (1964) 168.
26. A. Kuhn, M. Kunze, P. Sreeraj, H.-D. Wiemhöfer, V. Thangadurai, M. Wilkening, and P. Heitjans, Solid State Nucl. Magn. Reson. **42** (2012) 2.
27. M. Wilkening and P. Heitjans, Phys. Rev. B **77** (2008) 024311.
28. V. Epp and M. Wilkening, Phys. Rev. B **82** (2010) 020301.
29. A. Kuhn, P. Sreeraj, R. Pöttgen, H.-D. Wiemhöfer, M. Wilkening, and P. Heitjans, J. Am. Chem. Soc **133** (2011) 11018.
30. D. C. Look and I. J. Lowe, J. Chem. Phys. **44** (1966) 2995.
31. C. A. Sholl, J. Phys. C Solid State **14** (1981) 447.
32. R. E. Walstedt, Phys. Rev. Lett. **19** (1967) 146.